

RICE UNIVERSITY

Refinement of the strontium molecular potential by
numerical computation of bound states

Will Huie

Houston, Texas
April, 2020

ABSTRACT

Refinement of the strontium molecular potential by numerical computation of bound states

Will Huie

This thesis describes an improved determination of the long-range parameters C_6 , C_8 , and C_{10} of the strontium ground state molecular potential, which carry particular significance to ultracold atomic physics. The numerical values of these parameters are determined by way of a gradient descent fitting algorithm applied to a previous model of the potential and recent photoassociation-spectroscopy measurements of the binding energies of weakly bound ro-vibrational states of various strontium-dimer isotopologues. The results presented in later chapters are found to substantially improve the potential's description of these states and others not included in the fitting data set.

Additionally, numerical methods for computing solutions to the time-independent Schrödinger equation governing these bound states of strontium dimers are discussed as the backbone of the procedure for fitting the molecular potential parameters to experimental data. Several methods are described and evaluated with respect to the accuracies of their computed solutions as well as their runtime efficiencies for a harmonic-potential test case. Further, the code implementing these methods is also made available to assist with potential future projects.

Using the improved molecular potential and numerical solving methods, the binding energy of the least-bound, $\nu = 62$, $\ell = 0$ level of the electronic ground state of the $^{87}\text{Sr}_2$ dimer is predicted to be 25.9(9) MHz. The ^{87}Sr isotope is the last of the naturally occurring strontium isotopes for which the binding energy of this state has not been measured. Hence, this prediction is expected to assist with future efforts to observe this state and use it for further ultracold atomic physics experiments.

ACKNOWLEDGEMENTS

The past four years of my life spent at Rice have really flown by. It's truly startling in a slightly surreal sort of way to think back and realize that, while my time here has probably taught me more than the sum of my knowledge when I matriculated, it's been, in a sense, *only* four years since then. But such is the nature of time, I guess. I'd like to take the time here to thank a number of people who have enriched my life over these years in ways that my studies never could.

First and foremost to my advisor, Professor Tom Killian. The frankness and dedication that I've observed in your work ethic have truly inspired me for my coming years in graduate school and beyond. The guidance you've given me has helped open my mind to new ways of thinking that are invaluable. I have a great respect for your driven, focused attitude and high standards of quality.

To my friends Joseph, Tommy, and Christian from here at Rice. You've been a constant source of enjoyment from quite nearly when we all matriculated, and I can't imagine my Rice experience without you. Thank you for humoring my half-baked philosophical musings and letting me share my teas with you while I beat your asses in Smash. And to my friends Ian and Nick beyond the hedges. I know I can always count on you for honest, earnest, and analytical conversations about all aspects of life.

Finally to my brother Andrew and my parents Tommy and Janet. It really is impossible to express in words how much I value all the love and support you've given me, but I know you all understand. Mom and Dad, I also know you're a little disappointed by how COVID-19 has affected commencement this year, but let me assure you that we'll have another opportunity to properly celebrate in a few more years.

Contents

Abstract	i
Acknowledgements	ii
1 Introduction	1
1.1 Strontium isotopes	1
1.2 Thesis overview	4
2 Examination of numerical methods	5
2.1 Description of methods	7
2.1.1 Matrix Numerov method	8
2.1.2 Two-sided shooting and renormalized Numerov methods	10
2.2 Evaluation of methods	13
3 Refinement of the strontium potential	16
3.1 Fitting procedure	17
3.2 Fit results	19
3.3 Discussion of results	21
3.4 Prediction of the $^{87}\text{Sr}_2$ least-bound state	22
4 Conclusion and recommendations for future work	25
Appendices	29
A Description of the strontium molecular potential	30
B Evaluation of the energy-wavefunction coupling method	31
C Notes on the codebase	34
D Parameter fitting by gradient descent	37

1 Introduction

Where analytical solutions to the Schrödinger equation in atomic physics have yet to be found, numerical computation offers a powerful way to probe and improve theoretical understandings of interesting properties of quantum mechanical systems. In cases where measurements have yet to be taken, numerical computation can likewise provide predictions to help guide experiments. For this thesis, numerical methods are applied to the understanding of ultracold atoms and molecules, the main focus of the Killian lab.

Recent developments in ultracold physics where atoms and molecules are characteristically cooled to temperatures on the order of 1 mK or lower have led to the creation of ultracold molecules and novel states of matter such as Bose-Einstein condensates and quantum degenerate Fermi gases. The methods of production and properties of these systems are governed by the scattering properties of their constituent atoms. For example, collisions between atoms are critical to the efficiency of the evaporative cooling processes used to reach the lowest temperatures and scattering interactions determine the equilibrium properties of a Bose-Einstein condensate such as its stability, spatial density, and overall shape [1, 2].

The macroscopic properties of these dilute, cold gases can be entirely derived from two-body interactions, which themselves are governed by the two-body molecular potentials. These interactions are particularly sensitive to the long-range van der Waals portion of the potential. Weakly bound diatomic molecules are also very sensitive to this region, so examination of the binding energies of these states can provide a great deal of information that is of interest for ultracold physics.

1.1 Strontium isotopes

Strontium is an alkaline-earth element with four naturally occurring isotopes, ^{84}Sr , ^{86}Sr , ^{88}Sr , and ^{87}Sr . Of these, the first three are bosonic and have zero nuclear spin while the last is fermionic with spin $I = 9/2$, and all of them have a ground-state electron configuration with a closed valence shell. These collectively make the strontium isotopes appealing candidates

for many experiments. To give a few examples: each isotope features excited states with long-lasting lifetimes making them useful to atomic clocks, the ^{84}Sr isotope allows for the creation of stable Bose-Einstein condensates, and the closed-shell structure means that the nuclear spin of the ^{87}Sr isotope near-perfectly decouples from electronic spin for the $^1\text{S}_0$ and $^3\text{P}_0$ states, making the fermionic isotope well-suited to quantum information processing [2]. Thus much work has been done to characterize these species, especially in the low-temperature limit.

Over the last few years, measurements have been made of the binding energies of weakly bound states of the three bosonic isotopes [3–5] by two-photon photoassociation spectroscopy, whereby a trapped ultracold gas of atoms is illuminated with two laser fields to pair free atoms in the gas into bound dimers. This is achieved by tuning the laser frequencies such that one field drives an excitation in a colliding pair of atoms up to a state in the excited molecular potential, while the other stimulates emission down to one in the ground-state molecular potential, as shown in fig. 1. Photoassociation is usually detectable as a loss of atoms from the sample. The difference in laser frequencies corresponding to maximal atom loss corresponds to the binding energy of the molecular state. The measurements presented in [3–5] provide the experimental data for the work in this thesis.

The current best model of the molecular potential is from Tiemann [6], in which a functional form of the Sr_2 molecular potential was determined by fitting parameters in the form to the energies of the two weakly bound states of $^{88}\text{Sr}_2$ reported in [5] (those of $^{86}\text{Sr}_2$ and $^{84}\text{Sr}_2$ were not available at the time) along with the energies of nearly 15,645 transitions from electronic excited states to various ro-vibrational ground states of the $^{88}\text{Sr}_2$, $^{86}\text{Sr}^{88}\text{Sr}$, and $^{87}\text{Sr}^{88}\text{Sr}$ isotopologues measured by Fourier-transform spectroscopy. Though much of the potential was determined, the data set used was heavily biased towards the lower vibrational levels, as shown in fig. 2. The transition energies encompass states up to only the $\nu = 60$ vibrational level (these molecules reach a physical maximum at $\nu = 62$) with just 18 reaching $\nu \geq 58$. Since the more deeply bound states of these molecules are not strongly

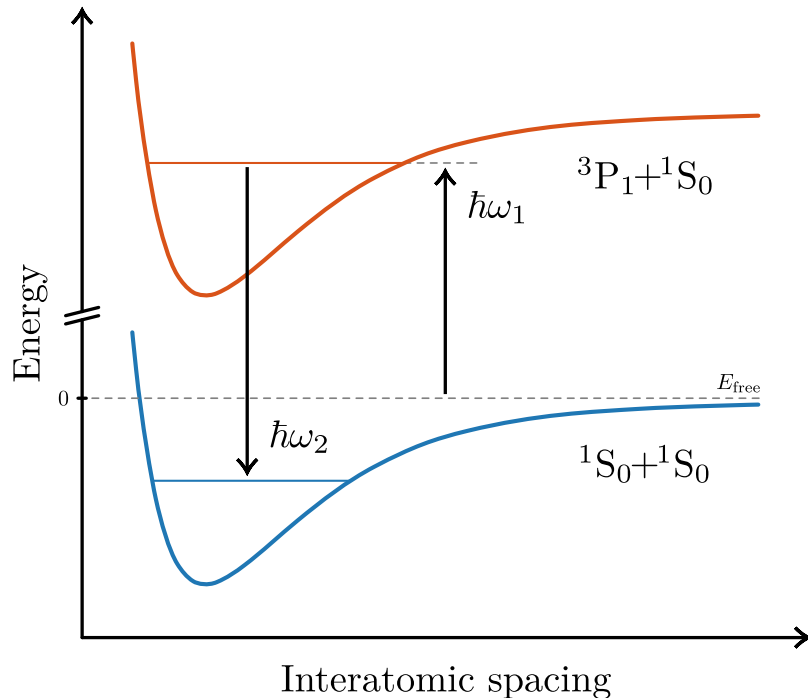


Figure 1: The two-photon photoassociation process between two atoms colliding with energy E_{free} on a ground state potential. One laser field tuned to frequency ω_1 initially excites the pair of atoms up to a state in an excited molecular potential (in orange) before the other field tuned to ω_2 stimulates emission down to a state in the ground-state potential (blue). The binding energy of the final state is the difference in laser energies, $E_b = \hbar|\omega_2 - \omega_1|$.

affected by the molecular potential at large distances, this means the potential's long-range features, which are of interest to ultracold physics, are comparatively poorly determined.

Now that more measurements of the binding energies of weakly bound states of various strontium dimers have been taken, however, this long-range strontium molecular potential can be better determined. This thesis employs a straightforward strategy to use the measurements of the $^{84}\text{Sr}_2$ and $^{86}\text{Sr}_2$ binding energies that were unavailable to Tiemann (along with the $^{88}\text{Sr}_2$ binding energies that were) to improve the potential using Tiemann's original formulation as a base. By solving the Schrödinger equation for the potential at vibrational and rotational quantum numbers corresponding to those measured, the extent to which the potential is able to describe the measured molecular states can be judged quantitatively and hence used to refine it as a numerical model. The resulting improved potential can then be used to generate a prediction of the binding energy of the $^{87}\text{Sr}_2$ dimer's least-bound state in order to assist with future experimental efforts.

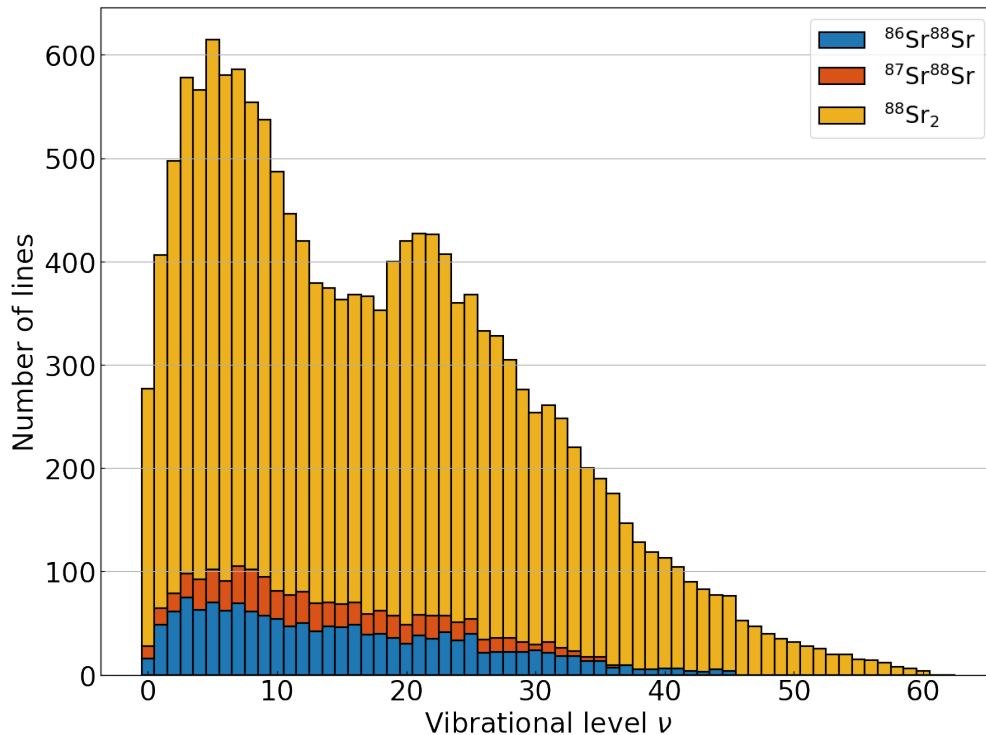


Figure 2: Distribution of the 15,645 transition energies used in Tiemann’s analysis among the various vibrational levels of the $^{88}\text{Sr}_2$, $^{86}\text{Sr}^{88}\text{Sr}$, and $^{87}\text{Sr}^{88}\text{Sr}$ isotopologues they belong to. The maximum vibrational level reached in the data set is $\nu = 60$, while the maximum physically attainable for the isotopologues is $\nu = 62$. Only 18 or about 0.1% of these data lie within the top five physically possible levels. Not pictured here are the two additional $\nu = 62$ states measured by photoassociation spectroscopy or the distribution of these transition energies among various ℓ rotational quantum numbers.

1.2 Thesis overview

In this thesis, a number of numerical techniques are leveraged to calculate the energy levels of ro-vibrational ground state molecules of various strontium isotopes and the long-range properties of the underlying molecular potential. Chapter 2 outlines the various numerical methods included in the tool that was developed and usefulness to this particular project. Chapter 3 presents the results of applying these methods to adjust selected parameters of Tiemann’s molecular potential to fit the binding energies of states in strontium dimers. Finally, chapter 4 will provide concluding remarks along with recommendations for future work.

2 Examination of numerical methods

The core of the work done in this thesis lies in the numerical methods used to find the energies of bound states for the strontium molecular potential. The governing equation considered here is the time-independent radial Schrödinger equation, written in the form

$$\frac{\partial^2 u}{\partial r^2} = -Q(r)u, \quad Q(r) = \frac{2\mu}{\hbar^2} \left(E - V(r) \right) - \frac{\ell(\ell + 1)}{r^2} \quad (1)$$

with μ as the reduced mass of the diatomic molecule, ℓ the rotational quantum number, and $V(r)$ the spherically symmetric molecular potential following the form shown in appendix A with zero chosen to be the energy of two atoms separated by a large distance at rest, $V(r \rightarrow \infty) = 0$. In numerical calculations, a discrete grid of N radial coordinates r_i are defined, and the values of the wavefunction $u_i = u(r_i)$ are computed usually by means of a linearized, discretized form of eq. 1. While a method to solve for u_i may choose a non-uniform spacing between coordinates, the methods used in this work require r_i taken to be spaced by a constant distance δr , formally defined as

$$r_i = r_0 + i\delta r, \quad i = 0, 1, \dots, N - 1 \quad (2)$$

for some chosen left-hand boundary r_0 .

Careful considerations must be made when choosing the values of r_i , due to two main features of the Schrödinger equation. The first is that for energies that are large compared to local features of the potential – regions where $Q(r)$ is large and positive – the wavefunction solutions oscillate over small length scales. To properly resolve these oscillations, a sufficiently small grid spacing must be used. The wavelength of a solution to eq. 1 can be considered as a function of the radial coordinate, $\lambda(r) = 2\pi/\sqrt{Q(r)}$ when $Q(r)$ is positive, and reaches a minimum value when $Q(r)$ reaches a maximum. Since all bound states for the strontium molecular potential lie below zero energy, the minimum value attained by $\lambda(r)$ for $E = 0$ gives a lower bound on the length scale of oscillations in the wavefunction of any bound state

for the potential. Thus for this thesis the grid spacing δr is chosen to be one fifteenth of this value,

$$\delta r = \frac{1}{15} \times \frac{2\pi}{\sqrt{2\mu|V_0|/\hbar^2}} \quad (3)$$

where the maximum value of $Q(r)$ in the $E = 0$ case has been simplified to $2\mu|V_0|/\hbar^2$, the absolute value of the potential minimum scaled by $2\mu/\hbar^2$.

The second feature that must be considered is the exponential decay of wavefunction solutions that occurs in classically forbidden regions and has characteristic length $q(r) = 1/\sqrt{|Q(r)|}$. In the case where $Q(r)$ in these regions is small and negative, $q(r)$ is large, giving the corresponding wavefunction large extensions beyond the classical turning point. But when calculating a wavefunction solution, the grid over which the wavefunction is calculated is necessarily finite, and the usual boundary conditions imposing $u \rightarrow 0$ as $r \rightarrow \infty$ must be replaced with zero-value conditions at the edges of the grid. Thus the boundaries of the radial coordinate grid must be chosen far enough into classically forbidden regions that the zero-value condition is sufficiently similar to the limiting $u(r \rightarrow \pm\infty) = 0$ one. For the strontium molecular potential, the above case occurs in the outer forbidden region for states bound at energies close to $E = 0$. In this region, $V(r) \rightarrow 0$ in the limit as $r \rightarrow \infty$, so to minimize the computational load, $q(r)$ is approximated as a constant value q_0 using $V(r) = 0$ for a given energy, and the length r_{ext} of the coordinate grid's extension into the forbidden region is chosen to be seven times that value,

$$r_{\text{ext}} = 7q_0 = 7 \times \frac{1}{\sqrt{2\mu|E|/\hbar^2}} \quad (4)$$

such that the wavefunction is allowed to decay to approximately $\exp(-7) \approx 0.1\%$ of its value at the outer turning point. This problem is strongly mitigated for the inner forbidden region due to the rapid divergence of the molecular potential as $r \rightarrow 0$, where $Q(r)$ is negative and large. In this region, the exponential decay of the wavefunction occurs over a small characteristic length, and is found to be suitably modeled by setting the left-hand boundary of the coordinate grid to be $r_0 = 1 \text{ \AA}$.

2.1 Description of methods

While there exist many general methods to numerically solve second-order equations, Numerov's method [7] is specialized to equations of the form of eq. 1, and is found to produce accurate solutions. Over a grid of radial coordinates following eq. 2, Numerov's method relates the values of the wavefunction u_i by the discretization

$$\left(1 + \frac{\delta r^2}{12} Q_{i+1}\right) u_{i+1} = 2 \left(1 - \frac{5\delta r^2}{12} Q_i\right) u_i - \left(1 + \frac{\delta r^2}{12} Q_{i-1}\right) u_{i-1} \quad (5)$$

where $Q_i = Q(x_i)$. This second-order recurrence relation is quite accurate, featuring an error term of size $\mathcal{O}(\delta r^6)$. Given appropriate left-hand boundary conditions for the value of the wavefunction and its first derivative captured in the values of u_0 and u_1 , a straightforward application of eq. 5 to a naive shooting method chooses a value for the energy E and iteratively calculates successive values of u_i using the relation until the other end of the coordinate grid is reached in a process known as numerical integration. If, after the integration has terminated, the values of the wavefunction go to zero at the right-hand boundary, then a solution to the Schrödinger equation is detected. If not, a new value for E is generated, and the process repeats. A critical problem with this approach, however, is that in classically forbidden regions where Q_i is negative, the integration couples easily into the exponential growth term of the general solution to the Schrödinger equation, often leading to numerical overflow in the computation and ultimately making solutions difficult to detect.

This section provides descriptions of three methods to solve eq. 1 derived from Numerov's method that circumvent the numerical overflow problem described above through two distinct means. The first of the methods is the matrix Numerov method [8], while the latter two are variations of Johnson's log-derivative method [9]. All three methods are evaluated in section 2.2 with respect to accuracy and efficiency when applied to a harmonic potential test case. The method of energy-wavefunction coupling [10] was also considered for this thesis, but ultimately discarded for reasons detailed in appendix B. All methods are implemented in an open-source Python library detailed in appendix C.

2.1.1 Matrix Numerov method

The matrix Numerov method [8] is computationally the simplest of the three methods discussed in this section. This method avoids numerical overflow by treating eq. 5 holistically as a set of N coupled linear equations. Rearranging the terms of the equation gives a $N \times N$ matrix eigenvalue equation

$$H\mathbf{u} = \left[-\frac{\hbar^2}{2\mu} B^{-1} A + V \right] \mathbf{u} = E\mathbf{u} \quad (6)$$

with \mathbf{u} being the column vector of u_i wavefunction values, and the matrices A , B , and V defined as

$$A = (\mathbb{I}_{-1} - 2\mathbb{I}_0 + \mathbb{I}_1) / \delta r^2 \quad (7)$$

$$B = (\mathbb{I}_{-1} - 10\mathbb{I}_0 + \mathbb{I}_1) / 12 \quad (8)$$

$$V_{ij} = \left(V(r_i) + \frac{\ell(\ell+1)\hbar^2}{2\mu r_i^2} \right) \delta_{ij} \quad (9)$$

Where \mathbb{I}_k denotes the matrix of size $N \times N$ with elements equal to one on the k -th diagonal ($k = 0$ being the main diagonal) and zero elsewhere. This approach is equivalent to expanding the state $|u\rangle$ on a basis of N Dirac delta function states $|r_i\rangle$ that have wavefunctions $\langle r|r_i\rangle = \delta(r-r_i)$ where the kinetic energy terms of each basis state as well as nearest-neighbor interactions between them are defined by Numerov's discretization. The amplitude of the $|r_i\rangle$ basis state is then the amplitude of the wavefunction of $|u\rangle$ at the corresponding grid point, $\langle r_i|u\rangle = u(r_i)$.

The choice of a finite, discrete basis of $|r_i\rangle$ states approximates the actual infinite, continuous one representing real space and implicitly assumes that the value of the wavefunction is zero everywhere outside the coordinate grid. This approximation is good to the extent that $u(r_i)$ does not change drastically between adjacent grid points and exponentially decays sufficiently close to zero at the grid boundaries. These conditions hold for δr small enough

with r_0 and r_{N-1} placed far enough into classically forbidden regions, and are equivalent to those detailed in the previous section.

Equation 6 can then be solved by calling one of the many existing numerical linear algebra libraries to calculate the N eigenvalues and eigenvectors of H that compose a superset of all bound-state solutions to the Schrödinger equation for the given potential. Generally, the first n eigenvalues and associated eigenvectors of lowest energy will correspond to the n physically realizable vibrational levels of the potential, while the rest can be discarded. If n is known, then the Schrödinger equation can be completely solved for the potential after a small additional step to sort and select solutions returned by the linear algebra routine. Additionally, many linear algebra libraries also feature routines that are optimized to compute only the eigenvalues of H , which saves a small bit of computing power if the wavefunction solutions are not needed.

The advantages of the matrix Numerov method lie in the straightforward process by which solutions to eq. 1 are found, and in the fact that all solutions can be found without any information about the system beyond a definition of the potential. Important downsides to the method arise from the need to construct and analyze a $N \times N$ matrix to find these solutions. This can be inefficient with respect to both runtime and memory in cases where N is large, with a time complexity of roughly $\mathcal{O}(N^3)$. While the solutions found by this method are accurate, as will be shown in section 2.2, this can be bad for applications where eq. 1 must be solved repeatedly, as is required for the strontium molecular potential refinement detailed in chapter 3. One other significant issue comes from the fact that the length scale over which wavefunctions oscillate decreases with increasing energy. As discussed for eq. 3, the coordinate grid over which solutions are calculated only needs to be dense enough to resolve these oscillations, meaning that grids for lower-energy solutions can be less dense than those for higher-energy solutions without significant loss to accuracy. But when eq. 5 is reformulated as a matrix eigenvalue equation, all solutions are necessarily calculated over the same grid, thus inefficiently allocating computing time. If only a small number of high-energy

solutions to eq. 1 are needed, then this entails adding substantial, unnecessary increases to total runtime.

2.1.2 Two-sided shooting and renormalized Numerov methods

In contrast to the matrix Numerov method, the two-sided shooting method and the renormalized Numerov method make use of a reformulation of the Numerov discretization, due to Johnson [9], that gives a specialized numerical integration scheme designed to avoid the numerical overflow problem described above. In this reformulation, the quantities $R_i = R(r_i)$ and $\tilde{R}_i = \tilde{R}(r_i)$ at each radial coordinate are defined as

$$R_i = \frac{(1 + \frac{\delta r^2}{12} Q_{i+1}) u_{i+1}}{(1 + \frac{\delta r^2}{12} Q_i) u_i} \quad (10)$$

$$\tilde{R}_i = \frac{(1 + \frac{\delta r^2}{12} Q_i) u_i}{(1 + \frac{\delta r^2}{12} Q_{i-1}) u_{i-1}} \quad (11)$$

Following a series of transformations performed on eq. 5 using these definitions, recurrence relations for both quantities can also be derived,

$$R_i = \frac{2 - 10 \frac{\delta r^2}{12} Q_i}{1 + \frac{\delta r^2}{12} Q_i} - \frac{1}{R_{i-1}} \quad (12)$$

$$\tilde{R}_i = \frac{2 - 10 \frac{\delta r^2}{12} Q_i}{1 + \frac{\delta r^2}{12} Q_i} - \frac{1}{\tilde{R}_{i+1}} \quad (13)$$

R_i and \tilde{R}_i are useful to calculate instead of u_i because, being defined as ratios between successive values of the wavefunction, they do not grow exponentially in classically forbidden regions and can be integrated from either the left or right boundaries of the coordinate grid using eq. 12 or eq. 13, respectively. Once R or \tilde{R} has been calculated, the values of the ‘true’ wavefunction u_i can be calculated up to a normalization factor using the definition of the counterpart quantity, either eq. 11 or eq. 10. Considering this, R and \tilde{R} are, in a sense, renormalized wavefunctions. When u_i is calculated in this way, no quantities are ever allowed to grow exponentially, and hence no risk of numerical overflow is ever encountered. In practice, R and \tilde{R} are integrated from opposite sides of the coordinate grid until the

integrations meet at a point r_M inside a classically allowed region, defined as the element of the radial coordinate grid of least value that is greater than the location of the wavefunction peak closest to the right-hand classically forbidden region (note that the Schrödinger equation forbid this peak from actually lying inside the forbidden region). The grid point r_M is mathematically characterized as the first coordinate encountered by the integration of \tilde{R} for which $\tilde{R}_i \leq 1$. If the energy of the wavefunctions is an eigenvalue of eq. 1 then the true wavefunctions calculated from the two integrations will be such that they can be matched smoothly at r_M .

To find the energies for which this will occur, the log derivative method – also due to Johnson [9] – is employed. In this method, the log derivative of the wavefunctions $y(r) = d \log u / dr = u'(r)/u(r)$ at the matching point r_M of the left- and right-integrations (y_l and y_r) are calculated. This quantity is useful to calculate because it captures both the value and the slope of the wavefunction as well as the relative sign between the two in a way that is independent of the wavefunction’s normalization. With this definition, it is easily seen that the energies for which the difference between the log derivatives of the left- and right-integrated wavefunctions vanishes are those for which the wavefunctions can be matched smoothly. In more precise terms, the energies where

$$D(E) = y_r(r_M) - y_l(r_M) \tag{14}$$

goes to zero are eigenvalues of eq. 1. The behavior of eq. 14 is shown in fig. 3. Qualitatively, the behavior of $D(E)$ is similar to that of the tangent function, where ranges of the input space are partitioned into regions characterized by the function increasing monotonically from negative infinity, crossing zero, then continuing on to positive infinity. Each of these partitions corresponds to a range of energies where wavefunctions will have a specific number of nodes – in other words, a locality surrounding a vibrational level.

The two-sided shooting and renormalized Numerov methods are identical in their use of eqs. 10–13 to integrate wavefunctions at given energies, but employ differing strategies to find the zeros of eq. 14. The shooting method offers a straightforward approach, where a

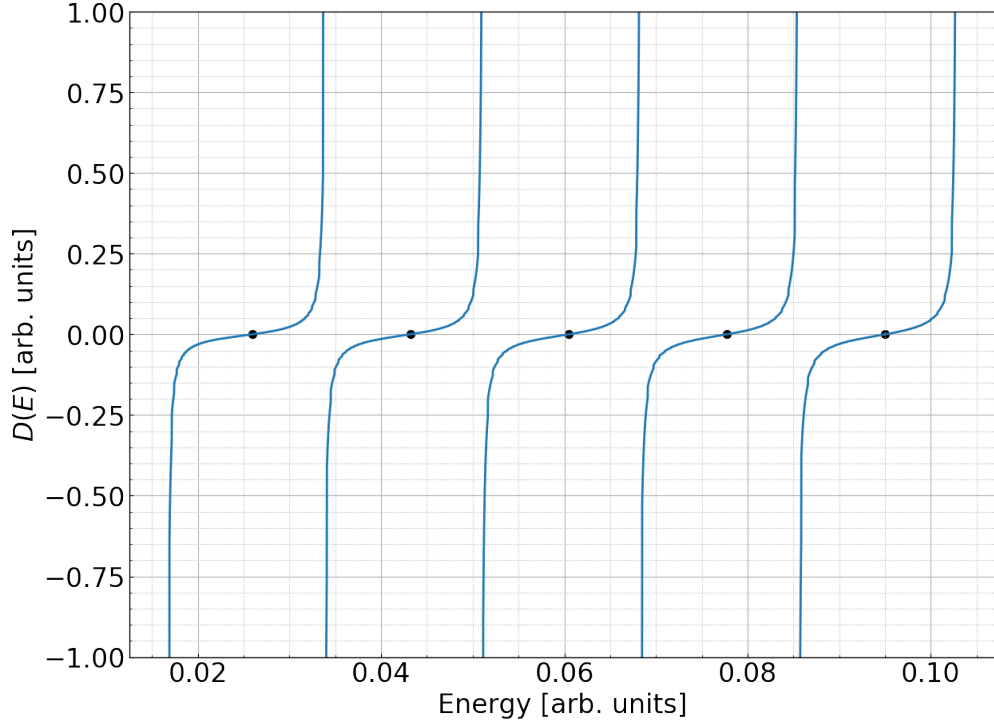


Figure 3: Equation 14 plotted versus energy for the test case of a harmonic potential. All quantities are in arbitrary units in order to show the qualitative behavior of the log derivative difference function. It is easily seen that $D(E)$ is partitioned into regions in which the function monotonically increases from negative infinity, crosses zero (marked by the black dots), and diverges to positive infinity. Each partition corresponds to wavefunctions with a particular number of nodes, with the zero in the partition corresponding to the exact energy of the associated vibrational mode.

grid of evenly spaced energy values is constructed, and the value of $D(E)$ is calculated at each one. Then, zeros can be found by interpolating Lagrange polynomials over appropriate subsets of this array of values. In contrast, the renormalized Numerov method employs a searching algorithm to find the zero corresponding to a specific vibrational level that works in two stages. The first stage generates two guess energies that are iteratively adjusted until they both lie in the partition corresponding to the desired vibrational level, which is verified by counting the nodes in the calculated wavefunctions as the number of times R is negative in the classically allowed region. The second stage then uses the secant method with evaluations of $D(E)$ at these guess energies to iteratively converge on the zero, with convergence detected when the difference between the two guesses meets a given accuracy goal.

The two-sided shooting and renormalized Numerov methods both feature the strong advantage of having runtime complexities that are linear in the size of the coordinate grid and are substantial improvements to the cubic complexity of the matrix Numerov method. These methods also provide ways to trade runtime for additional accuracy (or vice versa) by increasing the density of the energy grid in the case of the shooting method or decreasing the size of the accuracy threshold in the case of the renormalized Numerov method, without affecting the accuracy of the integrated wavefunction solution. The major downside to using these methods come from the fact that both require guessing information about the approximate values of the desired energy solutions, which may not generally be available prior to computation. Additionally, it is easily seen that the runtime of the shooting method is linear in the grid of energies over which it computes $D(E)$, making it typically unsuited to tasks involving a search for energy solutions that may be distributed over large ranges. Similarly, the renormalized Numerov method can only compute a single solution at a time, so it is likewise unsuited for computation of large numbers of energies.

2.2 Evaluation of methods

To test the performances of these numerical methods and ultimately determine which is most suited to the calculation of the energies of weakly bound strontium dimers, the methods were each applied to the test case of an electron in a harmonic potential, $V(x) = (1/2)m_e\omega^2x^2$ (with ℓ set to zero) where m_e denotes the electron free mass, and $\omega = 2\pi(10^{12})$ Hz. The energy eigenvalues of the vibrational levels for this potential follow the usual analytically derived formula, $E_n = \hbar\omega(n + 1/2)$.

Each method was used to compute the energies of the first fifteen vibrational levels ($n = 0, 1, \dots, 14$) for varied coordinate and energy grid sizes N_x and N_E . N_x and N_E were each varied independently while the other was held constant at a value of 1000 with coordinate grid boundaries set at $x = \pm 100$ nm and energy grid boundaries set at $E = E_0/2$ and $E = E_{14} + E_0/2$. The choice of spatial boundaries places them far enough into the classically forbidden regions that the accuracies of the calculated solutions were not

significantly impacted and the choice of energy grid boundaries gives a realistic simulation of the case where the values of the desired energy solutions are approximately known. For each combination of grid sizes, the root-mean-square of the differences between the numerically and analytically computed solutions as well as the time needed to compute the energies as an average of five trials were recorded. The results are shown in fig. 4.

As expected, the runtime of the shooting method is linear in the sizes of both the spatial coordinate and energy grids, while the matrix Numerov runtime looks to be cubic in spatial grid size, and that of the renormalized Numerov method is linear. The matrix Numerov and renormalized Numerov methods are most accurate at large spatial grid sizes, and all three are comparable for large enough energy grid sizes. These metrics indicate that for the application of these methods to the calculation of the energies of a few weakly bound states of strontium dimers detailed in chapter 3, where the considerations discussed at the beginning of this chapter predict the need for large spatial grid sizes, the renormalized Numerov method will perform best.

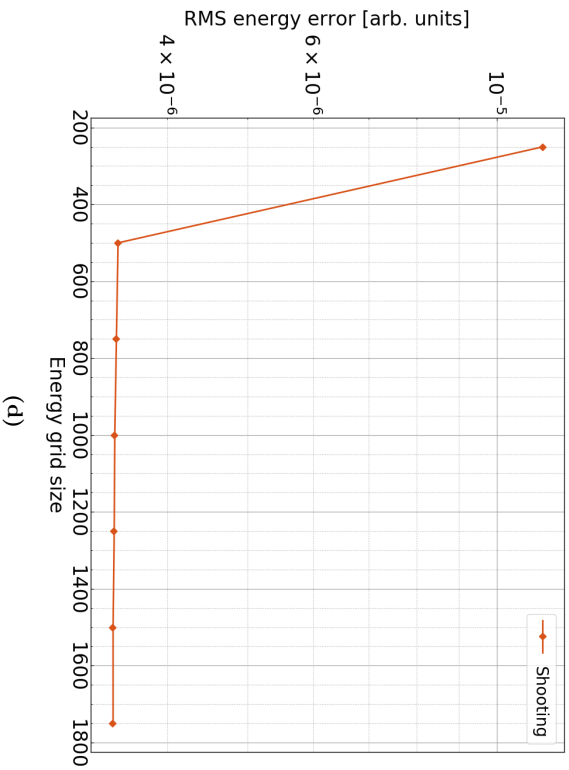
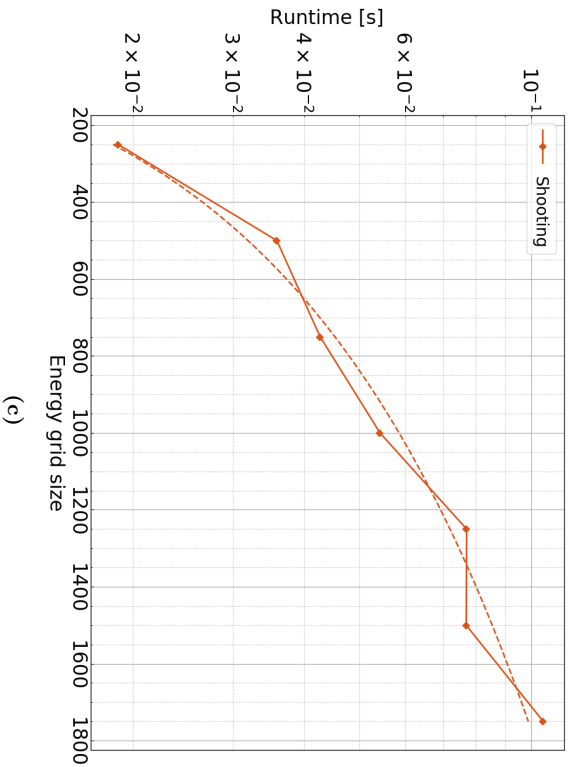
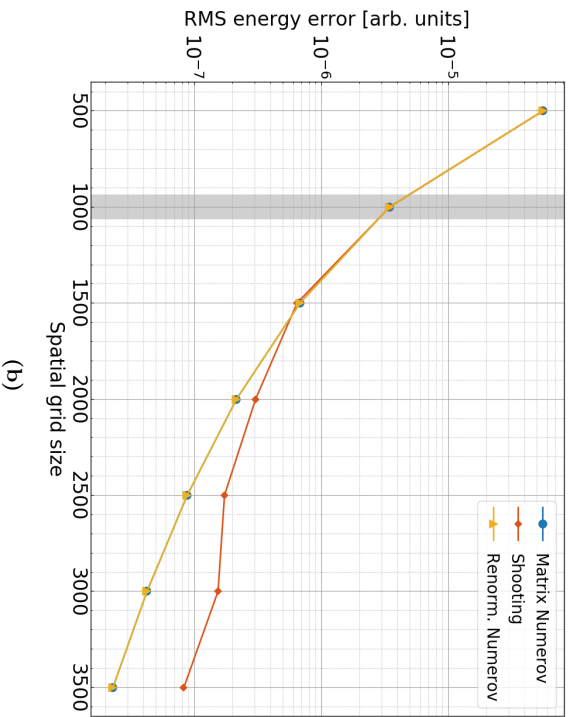
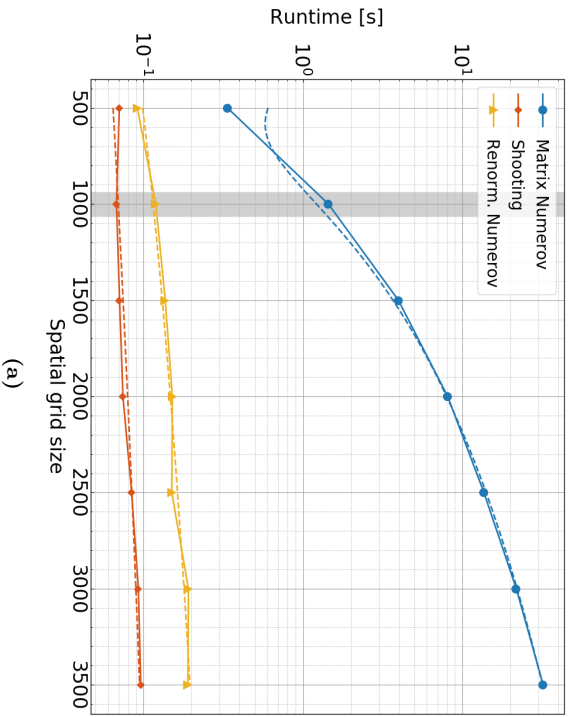


Figure 4: Benchmarks for the three numerical methods described in section 2.1 in terms of their runtimes (figs. 4a and 4c) and accuracies (figs. 4b and 4d), with respect to dependences on spatial coordinate grid size N_x (figs. 4a and 4b) and energy grid size N_E (figs. 4c and 4d). The dashed lines in the runtime plots are linear fits to the data shown in their respective colors, except for that of the matrix Numerov method in the upper-left plot, which is cubic. Gray bars in figs. 4a and 4b give the spatial grid size used in figs. 4c and 4d, $N_x = 1000$. The energy grid size used for the shooting method in ?? and fig. 4b is $N_E = 1000$. Accuracies are measured as the root-mean-square value of the differences between the first fifteen numerically and analytically computed energies for the harmonic potential in arbitrary units, while the runtimes are measured in seconds and taken as averages of five trials. Note that the matrix Numerov and renormalized Numerov methods give identical curves in fig. 4b.

3 Refinement of the strontium potential

To make a prediction of the $^{87}\text{Sr}_2$ binding energy, an accurate representation of the potential for the dimer states must first be determined. In [6], a functional form of this potential was found by fitting data from Fourier-transform spectroscopy of many transitions found in the ground states of the $^{88}\text{Sr}_2$, $^{86}\text{Sr}^{88}\text{Sr}$, and $^{87}\text{Sr}^{88}\text{Sr}$ isotopologues as well as the binding energies of two weakly bound states for $^{88}\text{Sr}_2$ measured by two-photon photoassociative spectroscopy [5]. The formula for the potential is a three-part piecewise-smooth function of the interatomic spacing comprising a short-range inner wall, a mid-range power law, and a long-range asymptote. The full form is detailed in appendix A.

The energies of six weakly bound states of the $^{84}\text{Sr}_2$ [3], $^{86}\text{Sr}_2$ [4], and $^{88}\text{Sr}_2$ [5] dimers are experimentally known and listed in table 1. Energies are stated with respect to the energy of the asymptote of two free atoms separated by a large distance at rest, giving negative energies for bound states. In this chapter, these data are compared to the numerical solutions to the Schrödinger equation for a potential of the form found in [6], and the resulting residuals are then used to fit potential parameters by way of a gradient descent algorithm described in appendix D.

The parameters n , C_6 , C_8 , C_{10} , A , B , and T_m , which determine various aspects of the short- and long-range portions of the potential, are adjusted by this method while the other parameters are held fixed at the values found in [6]. n controls the divergence rate of the inner wall diverging to positive infinity as the interatomic spacing r goes to zero, and C_6 , C_8 , C_{10} control the long-range asymptote as r goes to infinity. The dependent parameters A and B are used to maintain continuity and differentiability at the short- and mid-range junction of the potential while T_m is used to maintain continuity at the mid- and long-range junction.

The parameters of the long-range part of the potential, C_6 , C_8 , C_{10} , are the main focus of this thesis for two reasons. The first is that the new data included in this analysis compared to those of Tiemann's [6] set are weakly bound states, which strongly determine

these parameters. Tiemann did not have access to many data points in this regime, and his final potential was found to poorly predict the two $^{88}\text{Sr}_2$ states [5] that he did include. The values of the long-range parameters are significantly improved in this thesis. Second, the long-range part of the potential is critical for describing low-energy scattering and weakly bound states, which are of particular interest for ultracold physics, the main focus of the Killian lab. A , B , T_m , n are also investigated to determine sensitivity to any short-range part of the potential. The mid-range portion of the potential is neglected both to lessen the computational load on the fit and because the deeply bound states in the Tiemann analysis strongly determine the parameters of this part of the potential.

3.1 Fitting procedure

The parameters of the potential are determined by comparing the energies of each of the ro-vibrational states listed in table 1 to their corresponding values found by numerically solving eq. 1 in the case of the strontium molecular potential using a particular set of parameter values. The data set of measured energies is small and includes some points that are measured to high precision, so the renormalized Numerov method, which offers fast and precise calculation of specific vibrational levels as discussed in section 2.1, is used to complete this task. The comparison of numerical solutions to experimental data is done by way of a chi-squared value,

$$\chi^2 = \sum_i \frac{(K_i - M_i)^2}{\sigma_i^2} \quad (15)$$

where K_i and M_i are calculated and measured energy values, and σ_i are the uncertainties of the measurements.

Since the values of the parameters in the potential affect the energy solutions to eq. 1, χ^2 can be considered as a cost function of the parameters. Hence, the molecular potential is fit to the experimental data by minimizing the χ^2 cost function with respect to its parameters using the gradient descent algorithm outlined in appendix D. A strong advantage to this choice of cost function is that since χ^2 is a sum of quadratic terms, the constituent residuals

Species	ν	ℓ	Measured (Hz)	Original [6] (Hz)	Fit A (Hz)	Fit B (Hz)	Fit C (Hz)	Fit C diff. (Hz)
$^{84}\text{Sr}_2$ [3]	60	0	$-644.7372(2) \times 10^6$	-692.8439×10^6	-644.7036×10^6	-644.7455×10^6	-644.7393×10^6	-2.1344×10^3
	61	0	$-13.7162(2) \times 10^6$	-17.9150×10^6	-13.8023×10^6	-13.6885×10^6	-13.7195×10^6	-3.3477×10^3
	60	2	$-519.6177(5) \times 10^6$	-564.8159×10^6	-519.7949×10^6	-519.5766×10^6	-519.6013×10^6	1.6365×10^4
$^{86}\text{Sr}_2$ [4]	62	0	$-83.0(2) \times 10^3$	-438.0×10^3	-97.8×10^4	-88.2×10^3	-90.3×10^4	-7.29×10^3
$^{88}\text{Sr}_2$ [5]	62	0*	$-136.7(2) \times 10^6$	-155.0×10^6	-137.7×10^8	-137.2×10^6	-137.3×10^6	-5.561×10^5
	62	2*	$-66.6(2) \times 10^6$	-81.8×10^6	-67.7×10^6	-67.1×10^6	-67.2×10^6	-5.80×10^5
χ^2				6.647×10^{10}	3.446×10^5	2.842×10^4	2.809×10^3	

Table 1: Measured energies of weakly bound states in $^{84}\text{Sr}_2$, $^{86}\text{Sr}_2$, and $^{88}\text{Sr}_2$ compared to those calculated using the original potential parameter values given by Tiemann in [6] as well as from fits A, B, and C. Energies are stated with respect to the energy of the asymptote of two free atoms separated by a large distance at rest, giving negative energies for bound states. χ^2 values are reported for comparison between the measured and computed values. The rightmost column reports differences for energies calculated using fit C parameter values relative to measured counterparts. * indicates energies used by Tiemann.

of which vary monotonically with the chosen potential parameters, it can be seen that χ^2 is convex, implying that any local minimum of χ^2 found by the descent algorithm is also its global minimum. But since no analytical formula exists to precisely characterize eq. 15's dependence on the parameters, the partial derivatives involved in the descent processes are taken numerically using a centered finite-difference formula,

$$\frac{\partial \chi^2}{\partial x_i^{(n)}} \approx \frac{\chi^2\left((1 + \varepsilon)x_i^{(n)}\right) - \chi^2\left((1 - \varepsilon)x_i^{(n)}\right)}{2\varepsilon x_i^{(n)}} \quad (16)$$

for a potential parameter x_i at the n -th step of the descent and ε small enough, typically on the order of 10^{-6} . The fitting procedure stops when $|\nabla \chi^2|$ is less than 10^{-3} , which we define as convergence.

3.2 Fit results

In the application of the gradient descent fitting procedure described in appendix D, three key features of the potential introduced difficulties that made a determination of globally optimal parameter values difficult to obtain. This section details three fits (labeled A, B, and C) that were performed. Fit A takes a naive approach to show how these difficulties affect the descent, while fits B and C implement different approaches to circumvent them. Tiemann's parameter values were used as initial guesses. The parameter values found by each fitting procedure to minimize χ^2 are compared in table 2.

The first of the mentioned features is that the location of the hand-off between the short- and mid-range portions of the potential originally defined in [6], $R_i = 3.963 \text{ \AA}$, placed the short range portion controlled by n entirely above zero energy, greatly reducing n 's effect on the desired energy calculations. To remedy this, R_i was moved to 4.0 \AA in fits A and B in order to have n more strongly influence the determination of the states listed in table 1. Second, significant correlations between the varied parameters were observed, in agreement with the findings of [6]. These correlations were not rigorously characterized but were found in practice to reduce the overall effectiveness of the descent algorithm. The third feature

that impacted the fitting procedure was found to be a large variance in the strengths of the cost function’s dependences on the targeted potential parameters. In particular, the cost function was strongly dependent on n and weakly dependent on C_8 and C_{10} .

Since gradient descent is a so-called greedy algorithm – in that it chooses the path of steepest descent at every iteration – descents including potential parameters that strongly affect the cost function show minimization mainly with respect to those parameters, while leaving others mostly unaffected. This makes the results highly dependent on the initial guess of the descent as well as the criteria used to determine convergence. Fit A, a straightforward fit of n , C_6 , C_8 , and C_{10} , largely ignores C_6 , C_8 , and C_{10} by virtue of this fact, and pushes the value of n up to a large, unphysical value.

Fit B attempts to solve this problem by breaking the fit into three stages. In the first stage, only the parameters C_6 , C_8 , C_{10} on which χ^2 has comparatively weak dependence are subject to the descent; in the second, the first-stage parameters are held constant at their minimized values while n is fit; in the third, all parameters are included in a final descent together using their final values from the previous stages.

In fit C, n is fixed (with R_i reverting to its original value) and the fit of C_6 , C_8 , and C_{10} is split into five stages. In the first stage, all three parameters are varied together. To circumvent the effects of the cost function’s relatively weak dependence on C_8 and C_{10} , the initial guess values of these parameters are displaced by some δ to increase the sizes of their respective contributions to the gradient. The value of δ does not need to be small, but $\delta = -0.6\%$ was found to work well in practice. In the second and third stages, the number of variables included in the descent is reduced down to C_8 and C_{10} , then only C_{10} respectively. For the remaining two stages, the process is repeated in reverse order with the fourth stage fitting C_8 and C_{10} again and the fifth finally fitting all three. Every stage following the first begins with the minimizing parameter values found in the previous stage.

The main advantage to using the approach taken by fit C is that the minimum value of χ^2 it finds is, by approximately an order of magnitude, the smallest of the three fitting approaches described here, as shown in table 1. By this measure, the results of fit C (table 2)

give the best model of the strontium potential. Among the downsides is firstly that n is not varied, and so the sensitivity of the targeted states to the short-range portion of the potential is not accounted for. But if it were included in the first stage of fit C a problem similar to the one found in fit A would be encountered. The second downside to the approach of fit C is that the value of δ is somewhat arbitrarily chosen and requires manual experimentation to find. With a little clever automation, however, this can likely be mitigated.

It must be noted in table 2 that fits A, B, and C do not give the same final values of the fit parameters. Thus it cannot be concluded that the global minimum of the cost function has been found. As such, no estimations of systematic uncertainties can be made. The quoted uncertainties for the freely varied parameters n , C_6 , C_8 , C_{10} are the amounts by which each parameter must change in order to increase χ^2 by 25% of its minimized value. Correlations between parameters are not considered in this calculation.

Parameter	Original [6]	Fit A	Fit B	Fit C
R_i (Å)	3.963	4.0	4.0	3.963
n	12.362	65.26(8)	12.36(2)	12.362
C_6 (10^7 cm $^{-1}$ Å 6)	1.525(5)	1.52500(2)	1.516207(4)	1.5182802(5)
C_8 (10^8 cm $^{-1}$ Å 8)	(5.159)	5.1590(2)	5.15899(5)	5.128046(9)
C_{10} (10^{10} cm $^{-1}$ Å 10)	1.91(27)	1.9100(3)	1.91000(7)	1.89854(2)
T_m (cm $^{-1}$)	-1081.6384	-1081.6386	-1081.5730	-1081.5605
A (10^3 cm $^{-1}$)	-1.3328825	-3.6723791	-1.3583678	-1.3327952
B (10^{10} cm $^{-1}$ Å n)	3.321662099	$4.50612649 \times 10^{31}$	3.38924659	3.32203364
χ^2	6.648×10^{10}	3.446×10^5	2.842×10^4	2.809×10^3

Table 2: Original potential parameter values compared to those found via fits A, B, and C. Values of χ^2 for each set of parameter values are listed for comparison on the bottom row. Uncertainties for the parameter values from fits A, B, and C are given as statistical, estimated as the amount by which the parameter must change to cause an increase of 25% in χ^2 relative to its minimized value. Values without uncertainties are either exact, since their values are calculated from other parameters to maintain potential continuity (A , B , T_m), or fixed.

3.3 Discussion of results

In this section, fits A, B, and C are evaluated with respect to the quality of their predictions of the energies in table 1 as well as a subset (table 3) of the transition energies between more

deeply bound states used by [6] to generate the original values of the potential parameters. Full listings of the calculated transitions using the results of fits A, B, and C and the original parameter values are given in tables 1 and 3 respectively.

The subset of transition energies shown in table 3 are taken from a much larger set of 15,645 experimentally determined transition lines that were used in [6] along with the $^{88}\text{Sr}_2$ energies from [5] to determine the original potential parameter values. As such, the transitions and ^{88}Sr energies make for good points of comparison between the original and fit parameters. The chosen transition energies also serve as good evaluations of fits A, B, and C because they are an experimentally determined set of data outside the set on which the fits were trained. The specific transitions listed in table 3 were chosen as a representative subset of all those used in [6] and to measure how states more deeply bound in the potential may be affected by changes to the targeted potential parameters.

As shown in tables 1 and 3, fit C provides the best description of all the targeted energies and transitions by measure of the χ^2 and RMS error values listed. In particular, it improves the potential’s description of all the discussed weakly bound states, including the two $^{88}\text{Sr}_2$ states that were used in Tiemann’s data set. Fit C reduces the χ^2 value for these weakly bound energies by seven orders of magnitude. Fit C also improves the descriptions of more deeply bound states by measure of the transition energies in table 3, all of which were also used in Tiemann’s data set. Although convergence to the global minimum of the cost function was not established, it has nevertheless been shown that fit C offers a large improvement to the strontium molecular potential, making it the most suited to the calculation of the $^{87}\text{Sr}_2$ least-bound state in section 3.4. Considering this, the values of fit C (see table 2) are recommended for future works.

3.4 Prediction of the $^{87}\text{Sr}_2$ least-bound state

^{87}Sr is the last naturally occurring isotope of strontium for which the binding energy of the least-bound molecular state has not yet been measured. Like the other strontium isotopes (of mass numbers 84, 86, and 88), its position on the periodic table as an alkaline earth element

Transition ($\nu_1 \rightarrow \nu_2, \ell_1 \rightarrow \ell_2$)	Measured (cm^{-1})	Original (cm^{-1})	Fit A (cm^{-1})	Fit B (cm^{-1})	Fit C (cm^{-1})
24 \rightarrow 25, 8 \rightarrow 8	20.899	20.888	20.891	20.888	20.888
25 \rightarrow 26, 8 \rightarrow 8	20.149	20.148	20.153	20.149	20.148
26 \rightarrow 27, 8 \rightarrow 8	19.411	19.412	19.418	19.412	19.412
27 \rightarrow 28, 8 \rightarrow 8	18.679	18.680	18.686	18.680	18.680
28 \rightarrow 29, 8 \rightarrow 8	17.950	17.950	17.958	17.951	17.950
29 \rightarrow 30, 8 \rightarrow 8	17.220	17.225	17.233	17.225	17.225
30 \rightarrow 31, 8 \rightarrow 8	16.502	16.503	16.512	16.503	16.503
31 \rightarrow 34, 8 \rightarrow 8	45.200	45.211	45.244	45.212	45.211
34 \rightarrow 35, 8 \rightarrow 8	13.641	13.651	13.663	13.651	13.651
35 \rightarrow 36, 8 \rightarrow 8	12.942	12.948	12.959	12.949	12.948
36 \rightarrow 37, 8 \rightarrow 8	12.242	12.250	12.260	12.250	12.250
37 \rightarrow 38, 8 \rightarrow 8	11.548	11.556	11.566	11.556	11.556
38 \rightarrow 39, 8 \rightarrow 8	10.859	10.868	10.876	10.868	10.868
39 \rightarrow 40, 8 \rightarrow 8	10.175	10.185	10.192	10.185	10.185
40 \rightarrow 41, 8 \rightarrow 8	9.4981	9.5082	9.5133	9.5084	9.5082
41 \rightarrow 42, 8 \rightarrow 8	8.8282	8.8388	8.8419	8.8389	8.8388
42 \rightarrow 43, 8 \rightarrow 8	8.1660	8.1774	8.1784	8.1775	8.1774
43 \rightarrow 44, 8 \rightarrow 8	7.5130	7.5253	7.5240	7.5253	7.5253
44 \rightarrow 45, 8 \rightarrow 8	6.8714	6.2311	6.8803	6.8835	6.8836
45 \rightarrow 46, 8 \rightarrow 8	6.2411	6.9067	6.2487	6.2540	6.2542
46 \rightarrow 47, 8 \rightarrow 8	5.6256	5.6387	5.6314	5.6385	5.6387
47 \rightarrow 48, 8 \rightarrow 8	5.0261	5.0395	5.0305	5.0392	5.0395
48 \rightarrow 49, 8 \rightarrow 8	4.4455	4.4588	4.4483	4.4584	4.4587
49 \rightarrow 50, 8 \rightarrow 8	3.8878	3.8995	3.8880	3.8986	3.8989
50 \rightarrow 51, 8 \rightarrow 8	3.3541	3.3667	3.3546	3.3636	3.3632
51 \rightarrow 52, 8 \rightarrow 8	2.8493	2.8636	2.8510	2.8573	2.8559
52 \rightarrow 53, 8 \rightarrow 8	2.3778	2.3893	2.3767	2.3824	2.3811
53 \rightarrow 54, 8 \rightarrow 8	1.9424	1.9526	1.9404	1.9448	1.9435
54 \rightarrow 55, 8 \rightarrow 8	1.5421	1.5546	1.5431	1.5468	1.5456
55 \rightarrow 56, 8 \rightarrow 8	1.1889	1.1986	1.1881	1.1909	1.1900
56 \rightarrow 57, 8 \rightarrow 8	0.8769	0.8865	0.8772	0.8792	0.8785
57 \rightarrow 58, 8 \rightarrow 8	0.6088	0.6195	0.6115	0.6129	0.6124
58 \rightarrow 59, 8 \rightarrow 8	0.3913	0.3983	0.3918	0.3926	0.3922
59 \rightarrow 60, 8 \rightarrow 8	0.2196	0.2230	0.2179	0.2183	0.2181
Error RMS		9.107×10^{-2}	9.057×10^{-2}	8.069×10^{-2}	7.844×10^{-2}

Table 3: Measured $^{88}\text{Sr}_2$ transition energies compared to counterparts computed using the original potential parameter values from [6] as well as from fits A, B, and C. The root-mean-square values of the calculated–measured errors for each set of potential parameters are included for comparison.

gives it a closed-shell electron configuration. Unlike the other isotopes, however, its nucleus is fermionic with spin $I = 9/2$. This, in combination with its closed outer shell, makes it of interest to many potential experiments related to, for instance, degenerate Fermi gases, optical clocks, and quantum information processing [2]. Numerical calculation of the least bound state in $^{87}\text{Sr}_2$ is expected to assist with efforts to measure the state experimentally.

In section 3.3 it was shown that fit C provides the best descriptions of all the discussed energies and transitions. As such, it is also expected to give the best prediction of the $^{87}\text{Sr}_2$ least bound state. Using these parameter values and the renormalized Numerov method detailed in section 2.1, the $\nu = 62$, $\ell = 0$ ro-vibrational molecular state of $^{87}\text{Sr}_2$ in its electronic ground state is predicted to lie at $-25.9(9)$ MHz.

To estimate the uncertainty of this figure, the differences between the observed and calculated values of the binding energies for the weakly bound states (see the rightmost column of table 1) were considered as percentages of their corresponding measured values. The root-mean-square of these percentages, about 3.6%, was then considered to be the relative uncertainty of the above calculated binding energy. This number must be taken as a statistical uncertainty, as discussed in section 3.2.

4 Conclusion and recommendations for future work

This thesis presents a refinement to the theoretical understanding of the long-range strontium molecular potential. In ultracold physics, the main focus of the Killian lab, this aspect of the potential is of critical importance to describing the scattering properties of strontium, which lies at the heart of many interesting phenomena and potential experiments in the low-temperature limit [2]. Working from the results of an analysis completed previously by Tiemann [6], the values of parameters in the functional form of the potential were fit by a gradient descent algorithm to a data set of six measurements of weakly bound states of strontium dimers of various isotopes, four of which were not available to Tiemann.

Although this thesis was not able to show that the fit converged to the global optimum solution, the resulting new values of parameters in the potential nevertheless improved its descriptions of all bound states that were discussed by a considerable margin, including those used in Tiemann’s analysis. This work’s application of gradient descent to the potential-fitting problem reveals challenges for the algorithm’s formalism that arise from issues discussed in section 3.2. For future works seeking to continue the refinement of the potential’s parameters, a remedy may be found in a method of rescaling the parameters’ values such that the disparities in their contributions to the gradient of the cost function is reduced.

Work similar to this thesis has been done for isotopes of ytterbium [11]. In this analysis, the measured binding energies for bound states in ytterbium isotopes were fit via numerically computed solutions for these states to an effective molecular potential of the form

$$V(r) = -\frac{C_6}{r^6} \left(1 - \frac{\sigma^6}{r^6}\right) - \frac{C_8}{r^8} + B(r)J(J+1) \quad (17)$$

where the first term gives a Lennard-Jones potential, the last term involving $B(r) = \hbar^2/(2\mu r^2)$ is due to molecular rotation, and the C_8 term is the dipole-quadrupole interaction. Future

works may find a modified Lennard-Jones potential similar to eq. 17, possibly with an additional C_{10} term, more easily fit to the strontium experimental data.

Following the refinement of the molecular potential, the binding energy of the $\nu = 62$, $\ell = 0$ electronic ground state of the $^{87}\text{Sr}_2$ dimer was predicted to be $-25.9(9)$ MHz. The uncertainty in this prediction is estimated from the accuracies of the potential's descriptions of the other weakly bound states that were included in the fit. As such, it should be considered a statistical uncertainty, and is expected to improve easily with improvements to the fitting process. This prediction is hoped to be confirmed experimentally in the near future.

The work presented in this thesis has hopefully demonstrated the power and applicability of numerical computation. Although some issues arose in the implementation of the gradient descent algorithm, it is at any rate true that findings here have generated a significantly improved understanding of the strontium molecular potential and a prediction of the least-bound molecular state of the last strontium isotope for which this state's energy has not been measured. Accompanying this is the creation of a generalized tool to numerically solve the Schrödinger equation and assist with a wide variety of future projects.

References

- [1] Jean Dalibard, “Collisional dynamics of ultra-cold atomic gases,” in *Bose-Einstein Condensation in Atomic Gases*, Vol. 140 of *Proceedings of the International School of Physics “Enrico Fermi,”* p. 321–349. IOS Press Ebooks, 1998.
- [2] S. Stellmer, F. Schreck, and T. C. Killian, “Degenerate quantum gases of strontium,” in *Annual Review of Cold Atoms and Molecules*, p. 1–80. World Scientific, 2014.
- [3] S. Stellmer, B. Pasquiou, R. Grimm, and F. Schreck, “Creation of Ultracold Sr₂ Molecules in the Electronic Ground State.” *Phys. Rev. Let.* **109**:115302 (2012).
- [4] J. A. Aman, J. C. Hill, R. Ding, Kaden R. A. Hazzard, and T. C. Killian, “Photoassociative spectroscopy of a halo molecule in ⁸⁶Sr.” *Phys. Rev. A* **98**:22305 (2018).
- [5] Y. N. Martinez de Escobar, P. G. Mickelson, P. Pellegrini, S. B. Nagel, A. Traverson, M. Yan, R. Côté, and T. C. Killian, “Two-photon photoassociative spectroscopy of ultracold ⁸⁸Sr.” *Phys. Rev. A* **78**:062708 (2008).
- [6] A. Stein, H. Knöckel, and E. Tiemann, “The ¹S+¹S asymptote of Sr₂ studied by Fourier-transform spectroscopy.” *Eur. Phys. J. D* **57** (171) (2010).
- [7] B. Numerov, “Note on the numerical integration of $\frac{d^2x}{dt^2} = f(x, t)$.” *Astronomische Nachrichten* **230** (19) (1927).
- [8] M. Pillai, J. Goglio, and T. Walker, “Matrix Numerov method for solving Schrödinger’s equation.” *American Journal of Physics* **80** (11):1017–1019 (2012).
- [9] B. R. Johnson, “New numerical methods applied to solving the one-dimensional eigenvalue problem.” *J. Chem. Phys.* **67**:4086 (1977).
- [10] A. Udal, R. Reeder, E. Velmre, and P. Harrison, “Comparison of methods for solving the Schrödinger equation for multiquantum well heterostructure applications.” *Proc. Estonian Acad. Sci. Eng.* **12** (2006).

- [11] M. Kitagawa, K. Enomoto, K. Kasa, Y. Takahashi, R. Ciurylo, P. Naidon, and P. Julienne, “Two-color photoassociation spectroscopy of ytterbium atoms and the precise determinations of s -wave scattering lengths.” *Phys. Rev. A* **77**:012719 (2008).
- [12] J. Barzilai and J. M. Borwein, “Two-Point Step Size Gradient Methods.” *IMA Journal of Numerical Analysis* **8**:141–148 (1988).

APPENDICES

A Description of the strontium molecular potential

$$V(r) = \begin{cases} A + \frac{B}{r^n} & 0 \leq r < R_i \\ T_m + \sum_{i \geq 1} a_i \left(\frac{r - R_m}{r + bR_m} \right)^i & R_i \leq r \leq R_a \\ U_\infty - \frac{C_6}{r^6} - \frac{C_8}{r^8} - \frac{C_{10}}{r^{10}} & r < R_a \end{cases}$$

Parameters	
n	12.362
A	$-1.3328825 \times 10^3 \text{ cm}^{-1}$
B	$3.321662099 \times 10^{10} \text{ cm}^{-1} \text{ \AA}^n$
b	-0.17
R_m	4.6719018 \AA
T_m	$-1081.6384 \text{ cm}^{-1}$
a_1	$-6.50 \times 10^{-2} \text{ cm}^{-1}$
a_2	$1.5939056 \times 10^4 \text{ cm}^{-1}$
a_3	$-2.9646778 \times 10^4 \text{ cm}^{-1}$
a_4	$-6.6269777 \times 10^3 \text{ cm}^{-1}$
a_5	$4.4952358 \times 10^4 \text{ cm}^{-1}$
a_6	$8.709016 \times 10^3 \text{ cm}^{-1}$
a_7	$-1.0054929 \times 10^5 \text{ cm}^{-1}$
a_8	$5.94784152 \times 10^5 \text{ cm}^{-1}$
a_9	$-9.95239126 \times 10^5 \text{ cm}^{-1}$
a_{10}	$-1.14496717 \times 10^7 \text{ cm}^{-1}$
a_{11}	$4.606463055 \times 10^7 \text{ cm}^{-1}$
a_{12}	$3.74666573 \times 10^7 \text{ cm}^{-1}$
a_{13}	$-5.439157146 \times 10^8 \text{ cm}^{-1}$
a_{14}	$9.364833940 \times 10^8 \text{ cm}^{-1}$
a_{15}	$1.387879748 \times 10^9 \text{ cm}^{-1}$
a_{16}	$-8.4009054730 \times 10^9 \text{ cm}^{-1}$
a_{17}	$1.5781752106 \times 10^{10} \text{ cm}^{-1}$
a_{18}	$-1.5721037673 \times 10^{10} \text{ cm}^{-1}$
a_{19}	$8.376043061 \times 10^9 \text{ cm}^{-1}$
a_{20}	$-1.88984880 \times 10^9 \text{ cm}^{-1}$
C_6	$1.525 \times 10^7 \text{ cm}^{-1} \text{ \AA}^6$
C_8	$5.159 \times 10^8 \text{ cm}^{-1} \text{ \AA}^8$
C_{10}	$1.91 \times 10^{10} \text{ cm}^{-1} \text{ \AA}^{10}$
U_∞	0
R_i	3.963 \AA
R_a	10.5 \AA

Table 4: Numerical values of the parameters in the strontium potential taken from [6] reprinted here for convenience. Values are grouped by corresponding part of the potential.

B Evaluation of the energy-wavefunction coupling method

The core idea behind the energy-wavefunction coupling (EWC) method [10] lies in the construction of a vector quantity containing sampled wavefunction values as well as the energy of a poor initial guess solution to the Schrödinger equation. This composite vector is defined formally as

$$\mathbf{y} = (E, u_1, u_2, \dots, u_{N-1})^\top \quad (18)$$

where the guessed wavefunction values $u_i = u(r_i)$ over the grid follow the convention defined in chapter 2 and the wavefunction's energy E replaces the first of the sampled wavefunction values u_0 , since it is normally set to zero as a boundary condition. A second vector $\mathbf{F} = (F_0, \dots, F_{N-1})^\top$ evaluating the accuracy of \mathbf{y} as a solution to the Schrödinger equation is also defined as

$$F_i(\mathbf{y}) = \begin{cases} \sum_{i=1}^{N-1} [|u_i|^2 \delta r] - 1 & i = 0 \\ \frac{u_{i+1} - 2u_i + u_{i-1}}{\delta r^2} + Q_i u_i & 1 \leq i \leq N-2 \\ u_i & i = N-1 \end{cases} \quad (19)$$

with u_0 implicitly set equal to u_{N-1} . These quantities F_i compute the normalization integral of the guessed wavefunction for $i = 0$ as well as its compliance with the Schrödinger equation at each point and zero-value boundary conditions for $1 \leq i \leq N-2$ and $i = N-1$ respectively. If \mathbf{y} is a good solution, \mathbf{F} is zero.

With these considerations, a linear system subjecting \mathbf{y} to the constraint that \mathbf{F} tend to zero can be constructed and solved iteratively using Newton's method. For each iteration of the method, the solution \mathbf{y} is updated according to

$$\mathbf{y} = \tilde{\mathbf{y}} + \delta \mathbf{y}, \quad \left[\frac{\partial \mathbf{F}}{\partial \mathbf{y}} \right] \delta \mathbf{y} = -\tilde{\mathbf{F}} \quad (20)$$

where $\tilde{\mathbf{F}}$ is \mathbf{F} computed for the approximate solution $\tilde{\mathbf{y}}$, and $[\partial\mathbf{F}/\partial\mathbf{y}]$ is the Jacobi matrix containing the appropriate derivatives for the Newton method. Iteration can be halted when the magnitude of the corrections passes below some pre-set threshold. It is claimed in [10] that only 5-7 iterations are typically required for convergence.

Looking at eq. 19, it can be noted that the first term in F_i for $1 \leq i \leq N-2$ uses a centered finite difference formula as an approximation for the second-order partial derivative term in the Schrödinger equation, which is good up to a $\mathcal{O}(\delta r^2)$ error term. However, Numerov's method [7], whose derived methods are used to compute the initial guess wavefunctions and energies, features a much smaller error term that is $\mathcal{O}(\delta r^6)$. Thus when the EWC method is applied to these initial guesses, the Newton's method corrections $\delta\mathbf{y}$ are computed with greater error than the initial guess was to begin with, leading to an eventual *decrease* in the accuracy of the solution. Figure 5 shows the result of applying the EWC method to the solutions computed for the harmonic oscillator test case detailed in section 2.2 with an artificial cap on the number of Newton's method iteration set at 20. It can be easily seen that substantial increases in the errors of the of the calculated $n = 0$ and $n = 1$ energy solutions occur after the EWC method is applied. The solutions at larger n suffer similar increases in error that, while not as large as those of the first two solutions, show a significantly larger rate of increase as n grows compared to when the method is not applied.

Additionally, the application of the EWC method comes at the considerable cost of inverting an $N \times N$ matrix at each iteration of the Newton's method. When the energies of the desired solutions are large compared to a given potential's minimum, as in the case of the weakly bound states of strontium dimers, N is necessarily large in order to both resolve the fine oscillations of wavefunctions in classically allowed regions and account for large extensions into classically forbidden regions. Thus the use of this method becomes entirely untenable.

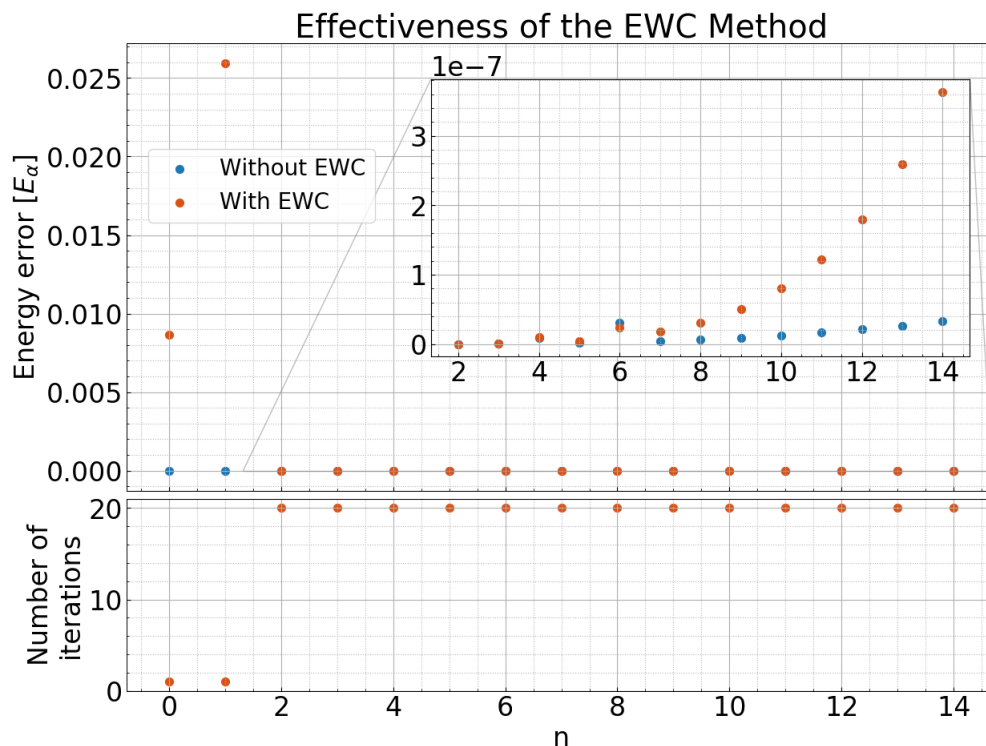


Figure 5: Errors of computed solutions to the Schrödinger equation for the harmonic oscillator test case described in section 2.2 that used the EWC method (orange), compared to those that did not (blue). Errors are measured as the absolute difference between the computed and analytical solutions' energies for a given vibrational level n in units of $E_\alpha = \hbar^2/2m_e\alpha^2$ for $\alpha = 10^{-9}$ m. Solutions computed with the EWC method show greater error that increases with growing n at a rate substantially greater than those without. The number of iterations

C Notes on the codebase

The numerical methods described in section 2.1 along with the gradient descent algorithm from section 3.1 and appendix D were implemented in Python. Python is a high-level, interpreted programming language that lends itself particularly to portability, making it a popular choice for scientific computation. The tools for this thesis are assembled in the form of a Python library called `libSr` hosted in a repository on GitLab at <https://gitlab.com/whoosie/srsolve>. (Despite the name, however, the library methods are generally applicable to any one-dimensional Schrödinger equation.) The repository’s `README` file and docstrings offer more exact usage directions for the constituent functions provided in the library.

The parts of the library used to accomplish the various components of this thesis are divided into sub-modules of `libSr`, with the most integral to this thesis being `libSr.solve`, `libSr.potential`, and `libSr.optim`. The `libSr.solve` module implements all the numerical methods described in chapter 2, and provides the `Solver` and `SrSolver` classes as the main interfaces to those methods. The former solves the Schrödinger equation for any potential function, while the latter provides additional class methods specialized to the strontium molecular potential. All computation performed in this module is with respect to scaled length and energy quantities $\tilde{r} = r/\alpha$ and $\tilde{E} = E/E_\alpha$ for $E_\alpha = \hbar^2/2\mu\alpha$, where α is a user-defined natural length scale (which itself should be provided in SI units) and μ is the reduced mass, to simplify relevant equations and reduce memory usage. `libSr.phys` provides convenient functions to convert between these scaled units and SI, as well as values of physical constants taken from the National Institute of Standards and Technology.

`libSr.potential` defines functions to compute Tiemann’s [6] strontium molecular potential from its analytical form, as well as its first and second derivatives. This module also provides convenient functions to compute quantities related to the potential such as its minimum, range, and outer turning point. The potential and its associated quantities can be calculated in either its given units (cm^{-1}) or α -scaled units. The `libSr.potentialMLR` module contains all of these functions for an alternative form of the strontium potential (also

given by Tiemann [6]) that at one point was considered for this thesis, but ultimately not used.

`libSr.optim` provides functions implementing the gradient descent algorithm used to fit the molecular potential. The main interface to this module is the `optim.optim` function, which drives the entire process of taking derivatives of the χ^2 cost function, computing step sizes, converging to the cost function minimum, and ultimately writing results to a file.

Finally, the auxiliary modules `libSr.interp`, `libSr.data`, and `libSr.misc` modules provide additional functions and data to support the operation of the main modules listed above. `libSr.interp` module provides functions for interpolating Lagrange polynomials and finding zeros that are needed by the two-sided shooting method. The smaller modules `libSr.data` and `libSr.misc` provide the experimental data found in table 1 and optional type-checking functionality for the library, respectively.

All of these modules are implemented in pure Python for maximum portability, but one significant consequence arising from this language’s dynamic typing and lack of a just-in-time (JIT) compiler is that tasks that involve large amounts of repeated computation, such as numerical integration and gradient descent, can be slower than when implemented in other systems that do feature JIT compilers like MATLAB and Mathematica. To overcome this while maintaining portability, `libSr.solve`, `libSr.potential`, `libSr.potentialMLR`, `libSr.interp`, and `optim`, which contain the library’s most computationally intensive functions, are also implemented in Cython as `*.pyx` files. Cython is an optimizing static compiler for both Python and the Cython programming language, which extends Python to add support for declaring static C types and calling C functions. When called, the Cython compiler generates and manages the compilation of C code from a Python or Cython source to produce equivalent (though much more efficient) C library extensions that are callable from a normal Python program. The end result is a substantial speed-up to the program at the cost of an initial compile step. The generated C code is additionally retained, allowing for the compilation of these C extensions even on systems that lack a Cython installation.

The following setup instructions apply to a standard BASH terminal. To use the library, the best-practice recommendation is to first create a python virtual environment before cloning the repository:

```
1 python -m venv srsolve_venv
2 cd srsolve_venv
3 source ./bin/activate
4 git clone https://gitlab.com/whooie/srsolve.git
```

The only true dependency needed for operation is NumPy, but users also may wish to install Matplotlib for plotting or Cython to compile C extensions. These are available from the Python Package Index.

```
5 python -m pip install numpy matplotlib cython
```

Then, if desired, the C extensions can be compiled with

```
6 python ./srsolve/setup.py build_ext --inplace
```

As mentioned above, they can also be compiled from the generated C files included in the repository using the provided makefile

```
7 cd srsolve
8 make
```

with the caveats that gcc must be installed (it must be sourced from outside the Python Package Index) and that changes made to the source *.pyx files will have no effect upon recompilation. Once this is completed, the elements of libSr can be imported from Python programs as normal.

D Parameter fitting by gradient descent

Gradient descent is an algorithm used to minimize a given function with respect to any number of variables. It is most famously known as the underlying mechanism by which machine learning models are trained, but is useful to this project for its simplicity and subsequent wide applicability.

The core of the algorithm revolves around the basic observation from multi-variable calculus stating that the direction of steepest increase in some function f of several variables in the small locality around \mathbf{x} is given by that of its gradient $\nabla f(\mathbf{x})$. It follows that the direction of steepest *descent* is the opposite, given by $-\nabla f(\mathbf{x})$. So given an initial guess vector \mathbf{x}_0 of arguments to the function, it is easy to see that iteratively updating \mathbf{x}_n according to

$$\mathbf{x}_{n+1} = \mathbf{x}_n - \gamma \nabla f(\mathbf{x}_n) \tag{21}$$

for $\gamma \in \mathbb{R}^+$ small enough will cause \mathbf{x}_n to converge towards the desired vector \mathbf{x}_{\min} that minimizes f . The main advantage to using gradient descent over other methods (for example regression methods) lies in its comparatively low need for sampling of $f(\mathbf{x})$, provided convergence times are short.

To improve convergence rates, γ (called the ‘step size’) is allowed to vary during the descent process according to a formula from [12],

$$\gamma \rightarrow L_n = \frac{|(\mathbf{x}_n - \mathbf{x}_{n-1}) \cdot (\nabla f(\mathbf{x}_n) - \nabla f(\mathbf{x}_{n-1}))|}{\|\nabla f(\mathbf{x}_n) - \nabla f(\mathbf{x}_{n-1})\|^2} \tag{22}$$

This variable step size was found to greatly improve the convergence rate of the descent in practice by alleviating problems arising from a constant step size being too small in early steps when the descent is far from the desired minimum, and too large in late steps when the descent is very close. In cases where the slope of f appears locally to be the same between successive steps of the descent, the denominator of eq. 22 is small, causing L_n to increase. This allows the descent to quickly traverse regions that would otherwise require a

large number of steps to cover. Conversely, when the slope of f appears to change rapidly between successive steps, L_n decreases, such that the descent is able to better resolve the shape of f . Then when the descent nears a minimum, ∇f is more likely to change directions between steps. Since the direction of a step taken (given by $\mathbf{x}_n - \mathbf{x}_{n-1}$) is in the direction of $\nabla f(\mathbf{x}_{n-1})$, the step and the change in the gradient misalign, causing the inner product in the numerator of eq. 22 to decrease. The overall effect is to decrease the size of L_n in order to avoid overshooting the minimum.